Aerodynamic Stability and Performance of Next-Generation Parachutes for Mars Descent

Keir C. Gonyea[1]
Georgia Institute of Technology, Atlanta, GA, 30332

Christopher L. Tanner[2] and Ian G. Clark[3]
Jet Propulsion Laboratory, California Institute of Technology, Pasadena, CA, 91109

Laura K. Kushner[4] and Edward T. Schairer[5]
NASA Ames Research Center, Moffett Field, CA 94035

Robert D. Braun[6]
Georgia Institute of Technology, Atlanta, GA, 30332

The Low Density Supersonic Decelerator Project is developing a next-generation supersonic parachute for use on future Mars missions. In order to determine the new parachute configuration, a wind tunnel test was conducted at the National Full-scale Aerodynamics Complex 80- by 120-foot Wind Tunnel at the NASA Ames Research Center. The goal of the wind tunnel test was to quantitatively determine the aerodynamic stability and performance of various canopy configurations in order to help select the design to be flown on the Supersonic Flight Dynamics tests. Parachute configurations included the disk-gap-band, ringsail, and ringsail-variant designs referred to as a disksail and starsail. During the wind tunnel test, digital cameras captured synchronized image streams of the parachute from three directions. Stereo photogrammetric processing was performed on the image data to track the position of the vent of the canopy throughout each run. The position data were processed to determine the geometric angular history of the parachute, which were then used to calculate the total angle of attack and its derivatives at each instant in time. Static and dynamic moment coefficients were extracted from these data using a parameter estimation method involving the one-dimensional equation of motion for a rotation of parachute. The coefficients were calculated over all of the available canopy states to reconstruct moment coefficient curves as a function of total angle of attack. From the stability curves, useful metrics such as the trim total angle of attack and pitch stiffness at the trim angle could be determined. These stability metrics were assessed in the context of the parachute's drag load and geometric porosity. While there was generally an inverse relationship between the drag load and the stability of the canopy, the data showed that it was possible to obtain similar stability properties as the disk-gap-band with slightly higher drag loads by appropriately tailoring the geometric porosity distribution.

[1] Graduate Research Assistant, School of Aerospace Engineering, keir@gatech.edu, AIAA student member
[2] Lead Test Engineer, christopher.l.tanner@jpl.nasa.gov, AIAA member
[3] LDSD Principal Investigator, ian.g.clark@jpl.nasa.gov, AIAA member
[4] Research Engineer, ACI/Experimental Aero-Physics Branch, laura.k.kushner@nasa.gov
[5] Aerospace Engineer, Experimental Aero-Physics Branch, edward.t.schairer@nasa.gov
[6] David and Andrew Lewis Professor of Space Technology, School of Aerospace Engineering, robert.braun@aerospace.gatech.edu, AIAA Fellow

Nomenclature

C_m	static moment coefficient
C_{m_0}	local intercept of static moment curve
C_{m_α}	local slope of static moment curve
$C_{m_{\dot{\alpha}}}$	dynamic moment coefficient
C_T	tangential force coefficient
D_0	parachute reference diameter
g	acceleration due to gravity
m	mass of the parachute canopy
M_{aero}	Moment due to canopy aerodynamics
Q_w	local dynamic pressure at the canopy
R_{cm}	distance from the ball joint to the canopy center of mass
R_{cp}	distance from the ball joint to the canopy center of pressure
R_v	distance from the ball joint to the canopy vent
S_0	parachute reference area
V_c	wind velocity at the canopy
V_w	wind velocity at the canopy corrected for canopy rotation
V_t	velocity of the canopy tangent to its arc of motion
x, y, z	wind tunnel frame coordinates (x streamwise, y lateral, z vertical)
α	angle of attack
α_G	total geometric angle
α_T	total angle of attack
β	sideslip angle
$\Delta\alpha$, $\Delta\beta$	dynamic contribution to the angle of attack and sideslip angle, respectively
γ	geometric angle between V_c and V_t
ϕ	clock angle (angle from vertical of wind tunnel axis projected onto yz-plane, positive clockwise)
θ, ψ	geometric pitch and yaw angles
Ω	magnitude of the angular velocity of the canopy

Subscripts

v	location of the canopy vent
θ	motion in the pitch plane
ψ	motion in the yaw plane
trim	trim angle of attack

Superscripts

’	parachute body axes

Acronyms

LDSD	Low Density Supersonic Decelerator
DGB	disk-gap-band
DS	disksail
NFAC	National Full-scale Aerodynamics Complex
PIA	Parachute Industry Association
RMS	root mean square
RS	ringsail
SS	starsail
TDT	Transonic Dynamics Tunnel

I. Introduction

The Low Density Supersonic Decelerator (LDSD) project is developing a next-generation supersonic parachute to be considered for use on future Mars missions. The resulting canopy design is expected to update or replace the disk-gap-band (DGB) parachute that has flown on all previous U.S. missions to the surface of Mars. Many

canopy variations were considered including ringsail and DGB parachutes as well as new designs referred to as disksail and starsail parachutes in order to understand the effects of distributing porosity throughout a canopy.[1]

LDSD quantified the stability characteristics of each canopy design through wind tunnel testing of sub-scale canopies (approximately 35% scale) with representative gore and ring structure. Static and dynamic aerodynamic coefficients (C_m and C_{m_α}, respectively) were estimated for each canopy as a function of total angle of attack (α_T). The aerodynamic coefficient curves were used to obtain stability metrics such as the trim total angle of attack and slope of the static aerodynamic curve at the trim total angle of attack for each canopy. These metrics help quantify the stability of each parachute so that they may be compared relative to one another.

Stability is an important factor in overall parachute performance. Chaotic motions of a parachute have the potential to disrupt guidance algorithms used to control the entry vehicle during descent and risk causing system instability. However, experimental determination of parachute aerodynamics is difficult because they are highly flexibly structures, have complex flow interactions, and exhibit apparent mass effects. A test in the NASA Langley Transonic Dynamics Tunnel (TDT) that was able to characterize some these effects by holding a textile parachute at the vent and rotating the parachute-payload system through a range of angles of attack.[2] While this test was technically more accurate than previous experiments using rigid parachute models, the error resulting from artificially holding the parachute at a constant angle of attack was not quantified. Moreover, this method of testing is not feasible in larger facilities such as NFAC due to the cost of constructing the necessary moving fixtures.

A second portion of the TDT test involved using a free flying parachute to determine drag performance.[2] A few years after the completion of the test, Schoenenberger et al. used video data from a downstream camera to extract the parachute stability coefficients.[3] By tracking the placement of the canopy vent in each video frame and transforming those data into a two-dimensional position in space, the total angle of attack and its first and second derivatives could be computed. These values were subsequently used in a parameter estimation methodology to calculate the static and dynamic aerodynamic coefficients at a given total angle of attack. The aerodynamics calculated for the DGB parachute correlated well with the static test results for the same canopy.[2] This parameter estimation methodology outlined in reference 2 is well suited to large-scale parachute testing and is the primary method being used to resolve the parachute stability characteristics.

Since the conversion of video data into parachute aerodynamics was not a primary objective of the TDT experiment, several approximations had to be made in order to compensate for the lack of some pieces of data. In particular, the use of a single downstream video camera caused ambiguity in the parachute location and the rapid motion of the canopy relative to the video frame rate induced error in the calculation of the angular rates and accelerations. The LDSD wind tunnel test attempted to improve knowledge of the parachute position by utilizing stereo photogrammetry and calculation of the angular derivatives were improved with data acquisition occurring at 60 Hz.

II. Test Setup

A. Canopy Description

LDSD tested a total of 4 different canopy types and a total of 13 different configurations.[1] The test articles had a nominal diameter (D_0) of 11.8 m (38.8 ft) and used a suspension line length of $1.7D_0$. The majority of the canopies were constructed from PIA-C-44378 "F-111" nylon broadcloth, which has a fabric permeability less than 5 $ft^3/min/ft^2$ per its specification. For the canopies constructed from F-111 nylon, the total porosity is assumed to be equal to the geometric porosity since the contribution from the fabric porosity is assumed to be negligible. The canopy designs that were tested are discussed below. Note that higher number rings are located further away from the canopy apex (closer to the canopy skirt).

1) Disk-gap-band: DGB canopies are constructed by separating a flat circular disk and a cylindrical band of fabric by an open gap to aid in stability. The DGB canopy serves as the reference by which all of the next-generation parachutes are assessed. Two configurations were tested:
    a. DGB-1: a flight spare of the parachute used for the Mars Phoenix Scout lander mission, constructed using MIL-C-7020 Type I nylon, which has a permeability of approximately 100 $ft^3/min/ft^2$. For this canopy, the contribution from fabric porosity is non-negligible and the total porosity was calculated to be between 12-18%.
    b. DGB-2: a replica of the Phoenix DGB constructed using F-111 nylon. This test article is shown in Fig. 1a.
2) Ringsail: ringsail parachutes are modifications of ringslot parachutes that add fullness to the fabric panels and allow for more airflow through the canopy. Five configurations were tested:

a. RS-0: a subscale version of a Ringsail parachute tested by JPL in 2005.[4] A picture of this test article is shown in Fig. 1b.
b. RS-1: the RS-0 canopy with two-thirds of ring 19 removed.
c. RS-2: the RS-0 canopy with 27% of rings 17, 18 and 19 removed.
d. RS-3: the RS-0 canopy with all of ring 19 removed.
e. RS-4: the RS-0 canopy with all of rings 18 and 19 removed.

3) Disksail: the disksail canopy is a modification of the Ringsail canopy that replaces the first ten rings around the canopy vent with a flat circular disk. The goal of this configuration was to decrease geometric porosity in the crown of the parachute to increase drag and allow that porosity to be redistributed to other portions of the canopy. Five configurations were tested:
   a. DS-1: the disksail as described above and as shown in Fig 1c.
   b. DS-2: the DS-1 canopy with half of ring 11 removed.
   c. DS-3: the DS-1 canopy with all of ring 11 removed.
   d. DS-4: the DS-1 canopy with all of ring 11 and half of ring 17 removed.
   e. DS-5: the DS-1 canopy with all of ring 11 and half of rings 17 and 18 removed.
4) Starsail: the starsail canopy is a modification of the Ringsail where multiple gores are replaced with a solid material creating a star pattern. The goal of this configuration is change how the geometric porosity is distributed throughout the canopy to retain drag and obtain some desirable stability characteristics. Portions of rings 17-20 were removed to obtain a geometric porosity approximately equal to the DGB. One starsail configuration was tested and is shown in Fig. 1d.

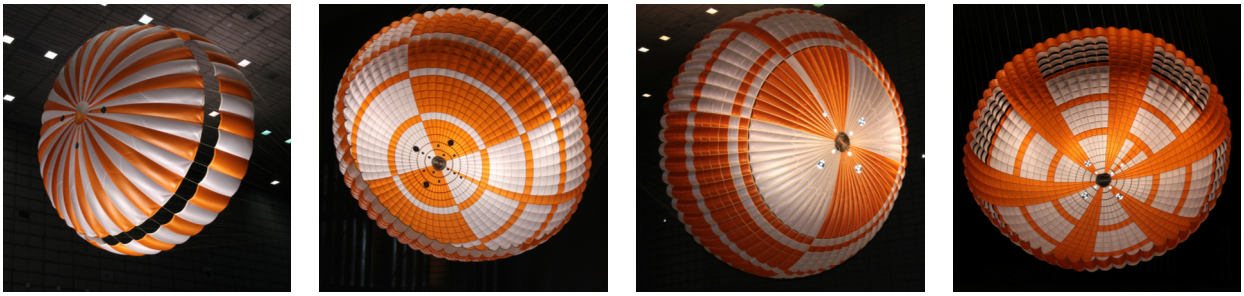

(a) disk-gap-band (b) ringsail (c) disksail (d) starsail

Figure 1. Primary canopy configurations used in NFAC testing.

Each canopy was equipped with fourteen retro-reflective targets on both sides of the canopy that appeared in high contrast against the test article and allowed for the canopy to be more easily tracked by the photogrammetry system described in Section II.C. Fiducial target material was carefully selected to maximize light return across a relatively broad range of incidence angles. Targets were located in three concentric rings around the vent with coded target patterns on the outer-most ring to resolve parachute roll about its axis of symmetry. The target pattern is shown in Fig. 2.

Figure 2. Retro-reflective target pattern on each test article.

B. Test Conditions

The wind tunnel testing was performed at the National Full-scale Aerodynamics Complex (NFAC) 80- by 120-foot (80x120) Wind Tunnel at the NASA Ames Research Center. Parachutes were fixed to a strut at the center of the test section via a load arm and ball joint. Mounted to the front of the strut was an aeroshell simulator, which was intended to approximate the wake generated by the forebody that will be present during future flight tests. This aeroshell simulator was fixed to the strut and was not allowed to move with the parachute. A diagram of the test setup can be seen in Fig. 3.

The canopies were tested at nominal freestream wind velocities of both approximately 15 and 25 kts. Pressure probes measured the dynamic pressure during the test and were located both upstream of the strut to measure the freestream conditions and downstream of the canopy skirt to measure blockage effects.

C. Photogrammetry System

1. Photogrammetry Setup

The purpose of the photogrammetry system was accurately measure the position of the test articles in three-dimensional space in order to estimate their static and dynamic stability characteristics. The photogrammetry hardware consisted of three high-resolution (2352x1728 pixels) synchronized cameras, two downstream of the parachute on the floor of the test section diffuser and one upstream of the parachute mounted on the strut just below tunnel centerline. The locations of the cameras and the choice of lenses were determined using virtual-imaging software to predict the camera views and ensure that the canopies would be visible over the expected range of positions.[5] The two downstream cameras were placed symmetrically near the corners of the test section to provide stereo imaging of the outer surface of the canopy. They were located sufficiently far downstream to be able to view the retro-reflective targets on the canopy at up to 20° total angle of attack in any direction. The upstream camera was mounted just below the riser attachment and provided a full view of the inside surface of the canopy. The cameras acquired images at 60 Hz – more than ten times the oscillation frequency of the parachute, thereby eliminating any aliasing of the canopy motion. High-intensity lamps were placed next to each camera to maximize the light output of the retro-reflective targets on the canopy and minimize the uncertainty in the position tracking. The photogrammetry configuration relative to the overall test set-up can be seen in Fig 3. A synchronized view from each of the photogrammetry cameras is shown in Fig. 4.

2. Photogrammetry Calibration

The biggest challenge in making photogrammetry measurements on such a large scale was calibrating the cameras. Therefore, two independent calibration methods were used, which provided verification for each other. The first and simplest method was the Direct Linear Transformation, which required first placing and focusing the cameras and then imaging at least six targets in the region of interest whose spatial coordinates were known.[6] The

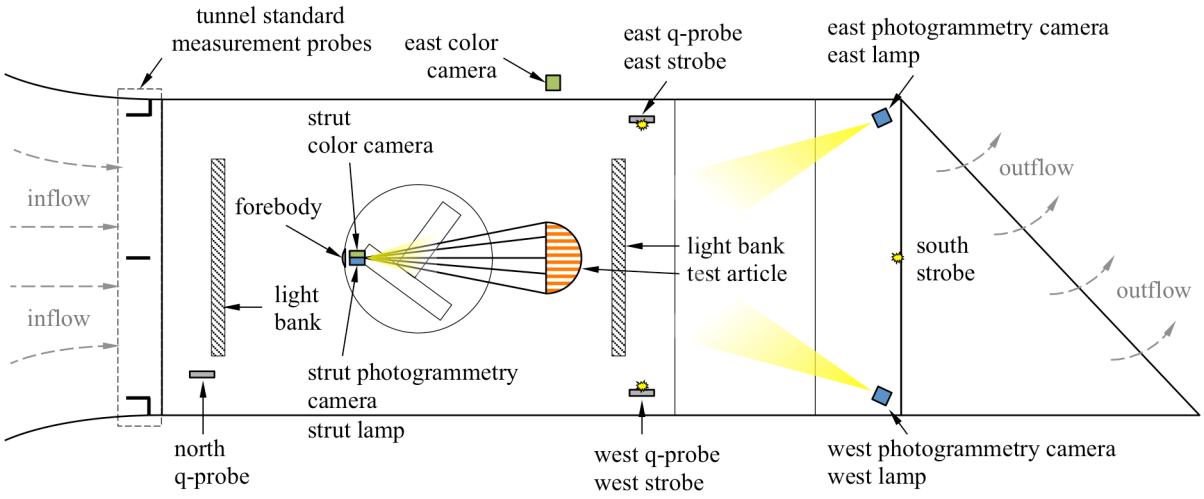

Figure 3. Planview of the wind tunnel test section.

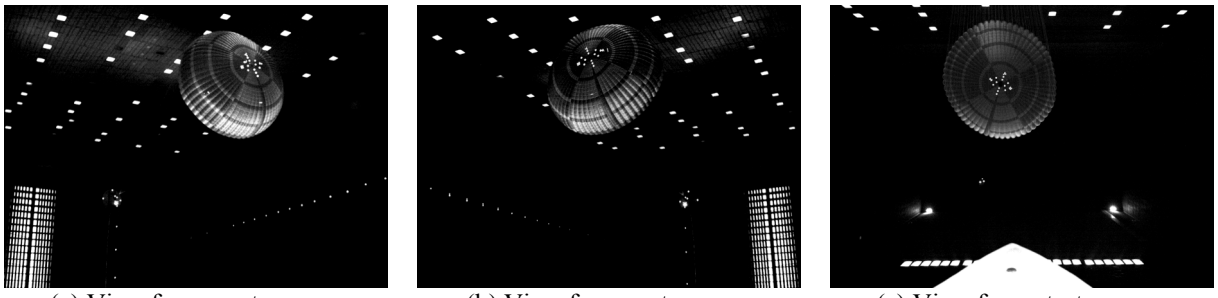

(a) View from west camera (b) View from east camera (c) View from strut camera

Figure 4. Synchronized images from the three photogrammetry camera views. Stereo photogrammetric measurements were computed using the east and west views.

second method required first measuring the "internal orientation" of each camera (focal length, lens distortion corrections, and location of the optical axis in the image plane) before the cameras were mounted. This was accomplished by acquiring images with each camera of a planar array of known targets. These targets were applied in a rectangular grid to one sidewall of the test section. Then, after the cameras were mounted in their final positions and pointed, the spatial positions and point angles of the cameras ("external orientation") were computed from images of a set of targets in the fields of view whose spatial coordinates were known.

Calibration targets were placed on a crane positioned in the region of interest, the strut fairing, and the test section sidewalls. The space coordinates of the calibration targets were precisely determined by imaging them from many directions using a commercial photogrammetry system. Both the Direct Linear Transform and internal/external orientation methods resulted in coefficients for each camera, which, together with image-plane coordinates of targets that appear in the images of at least two cameras, allowed computation of the space coordinates of the targets. Unlike the single-camera measurements used in reference 3 and previous photogrammetry measurements of parachutes in the 80x120,[7] the stereo imaging method used for this test allowed for accurate three-dimensional tracking of the vent without assuming a constant distance from the canopy to the point of rotation.

3. Photogrammetry Validation

The uncertainty in the photogrammetry system was determined by comparing the camera measurements of verification targets against their known coordinates. Measurements were made with the targets supported on a lift at three different heights and three different lateral locations at the streamwise position of the canopies. The relative error of the photogrammetry measurements was determined by first translating and rotating the measured coordinates of the targets to minimize the root mean square (RMS) difference with the true coordinates. The resulting minimum RMS error was less than half of an inch. The uncertainty in the absolute position of the targets was estimated by dangling a tape measure and plumb bob from the rig to the floor of the test section and then measuring to known reference points. Based on these measurements, the uncertainty in absolute position was less than one inch. These uncertainty estimates are consistent with the expected uncertainty due to a one-pixel error in locating targets in the images. The spatial position of the vent was calculated using both the Direct Linear Transformation and the internal/external calibration methods, resulting in similar coordinates. The internal/external calibration method was ultimately selected to generate all of the data herein.

III. Data Analyses

A. Canopy Vent Coordinates to Geometric Angles

Once the position history of the canopy was determined, the coordinates of the vent were converted into geometric angles, which are more convenient for describing the rotational motion of the parachute. Geometric angles are defined here as angles that are dependent only on the parachute's position with respect to the wind tunnel and do not take into account the parachute's motion with respect to the wind. A diagram showing the wind tunnel and parachute reference frames as well as the relevant geometric angles is shown in Fig. 4. The wind tunnel frame is denoted as $\{x, y, z\}$ and the parachute frame is denoted as $\{x', y', z'\}$ with the origin located at the ball joint, The parachute angular velocity is defined as Ω. The parachute and wind tunnel frames are related by a series of Euler rotations, first by the pitch angle (θ) about the y-axis, followed by the yaw angle (ψ) about the z'-axis. The full rotation matrix can be seen in Eq. (1).

$$\begin{bmatrix} x \\ y \\ z \end{bmatrix} = \begin{bmatrix} \cos\theta\cos\psi & -\cos\theta\sin\psi & \sin\theta \\ \sin\psi & \cos\psi & 0 \\ -\sin\theta\cos\psi & \sin\theta\sin\psi & \cos\theta \end{bmatrix} \begin{bmatrix} x' \\ y' \\ z' \end{bmatrix} \quad (1)$$

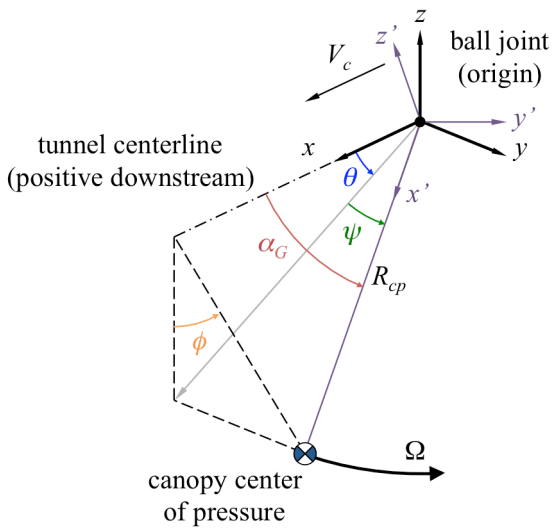

Figure 5. Wind tunnel and canopy coordinate systems.

The length of the parachute from the ball joint to the vent is defined as R_v. Knowing R_v and the $\{x_v, y_v, z_v\}$ coordinates of the canopy vent, the pitch and yaw angles can be calculated via Eqs. (3) and (4).

$$R_v = \sqrt{x_v^2 + y_v^2 + z_v^2} \tag{2}$$

$$\theta = \sin^{-1}\left(-\frac{z_v}{R_v \cos\psi}\right) \tag{3}$$

$$\psi = \sin^{-1}\left(\frac{y_v}{R_v}\right) \tag{4}$$

Two other geometric angles that are convenient to define are the total geometric angle (α_G) and clock angle (ϕ). The total geometric angle is the total angular distance between the parachute *x'*-axis and the wind tunnel *x*-axis. Note that the total geometric angle is not the same as the total angle of attack, which will be defined later. The clock angle describes the parachute position in the *yz*-plane when looking upstream. It is defined to be $\phi = 0$ when $y_v = 0$ and $z_v > 0$ and $\phi = \pi/2$ when $z_v = 0$ and $y_v > 0$. The total geometric angle and the clock angle can be calculated via Eqs. (5) and (6).

$$\alpha_G = \cos^{-1}\left(\frac{x_v}{R_v}\right) \tag{5}$$

$$\phi = \tan^{-1}\left(\frac{\sin\theta\cos\psi}{\sin\psi}\right) \tag{6}$$

1. Calculating the Total Angle of Attack and its Derivatives

The total angle of attack can be expressed in terms of the traditional angle of attack and sideslip as in Eq. (7). Note that the total angle of attack is always positive due to its physical definition.

$$\alpha_T = \cos^{-1}\left[\cos\alpha\cos\beta\right] \tag{7}$$

If the canopy is stationary, then the angle of attack is equal to the pitch angle, the sideslip angle is equal to the yaw angle, and the total angle of attack is equal to the total geometric angle. However, if the parachute is moving, then the rotational motion alters the local wind velocity at the canopy and introduces dynamic contributions ($\Delta\alpha$, $\Delta\beta$) to the geometric pitch and yaw angles, as in Eqs. (8).

$$\alpha = \theta + \Delta\alpha \tag{8.1}$$

$$\beta = \psi + \Delta\beta \tag{8.2}$$

Calculating the aerodynamic coefficients requires knowledge of the first and second derivatives of the total angle of attack with respect to time, which can be calculated using finite differencing. However, since α_T is always positive, its value can change very rapidly and potentially create non-smooth derivatives. An analytic method of calculating the first and second derivatives of the total angle of attack was developed that only requires finite differencing of the aerodynamic angles α and β. These angles have both positive and negative magnitudes and vary smoothly and periodically in time, making them well suited for differentiation via finite differencing. The first and second derivatives of the total angle of attack are given in Eqs. (9) and (10). Additional details regarding the calculation $\Delta\alpha$, $\Delta\beta$, and their respective derivatives are given in Appendices A and B.

$$\dot{\alpha}_T = \frac{\dot{\alpha}\sin\alpha\cos\beta + \dot{\beta}\cos\alpha\sin\beta}{\sin\alpha_T} \tag{9}$$

$$\ddot{\alpha}_T = \frac{\ddot{\alpha}\sin\alpha\cos\beta + \ddot{\beta}\cos\alpha\sin\beta + (\dot{\alpha}^2 + \dot{\beta}^2 - \dot{\alpha}_T^2)\cos\alpha_T - 2\dot{\alpha}\dot{\beta}\sin\alpha\sin\beta}{\sin\alpha_T} \tag{10}$$

B. Local Wind Velocity at the Canopy

The total wind velocity at the canopy is the vector sum of the freestream wind velocity ($\mathbf{V}_c$) and the velocity tangent to the canopy's arc of motion ($\mathbf{V}_t$). Note that the wind velocity resulting from the canopy's rotational motion is equal and opposite to the tangential velocity of the canopy, thus it is subtracted from the $\mathbf{V}_c$ as in Eq. (11.1). The total wind velocity (V_w) is the magnitude (L^2- norm) of the total wind velocity vector ($\mathbf{V}_w$) given in Eq. (11.2).

$$\mathbf{V}_w = \mathbf{V}_c - \mathbf{V}_t \tag{11.1}$$

$$V_w = \sqrt{\left(V_c - \dot{x}_{cp}\right)^2 + \dot{y}_{cp}^2 + \dot{z}_{cp}^2} \tag{11.2}$$

The velocity of the canopy tangent to its arc of motion can be expressed in terms of the Euler angles (See Fig. 4) as in Eq. (12). The canopy velocity is taken at the center of pressure (R_{cp}), which is where the aerodynamic forces are assumed to act.

$$\mathbf{V}_t = \begin{bmatrix} \dot{x}_{cp} \\ \dot{y}_{cp} \\ \dot{z}_{cp} \end{bmatrix} = R_{cp} \begin{bmatrix} -\dot{\theta}\sin\theta\cos\psi - \dot{\psi}\cos\theta\sin\psi \\ \dot{\psi}\cos\psi \\ -\dot{\theta}\cos\theta\cos\psi + \dot{\psi}\sin\theta\sin\psi \end{bmatrix} \tag{12}$$

C. Calculating the Aerodynamic Coefficients

The angular behavior with respect to the wind described in Section III.A can be used to determine the canopy stability coefficients using parameter estimation.[3] Given that the parachute is an axisymmetric body, the entire attitude history can be decomposed into motion in two directions - in the same direction as the total angle of attack and in the direction orthogonal to the total angle of attack. It is assumed in this analysis that the time-averaged aerodynamic coefficients in the direction orthogonal to the total angle of attack are zero. The only other necessary parameter is the clock angle ϕ, which is solely used to calculate the influence of gravity.

The aerodynamic moments on the parachute are represented as a static moment, dependent on the parachute's total angle of attack, and a dynamic moment, dependent on the instantaneous rate of change of the total angle of attack. The static moment curve is locally linearized at each total angle of attack into the pitch stiffness C_{m_α} and the moment at 0° total angle of attack C_{m_0}, as in Eq. (13.1). The resulting expression for the total aerodynamic moment is given in Eq. (13.2) where Q_w is the dynamic pressure accounting for canopy rotation, S_0 is the parachute reference area, and D_0 is the parachute reference diameter.

$$C_m = C_{m_\alpha}\alpha_T + C_{m_0} \tag{13.1}$$

$$M_{aero} = Q_w S_0 D_0 \left[C_{m_{\dot{\alpha}}} \frac{D_0}{2V_\infty}\dot{\alpha}_T + C_{m_\alpha}\alpha_T + C_{m_0} \right] \tag{13.2}$$

The one-dimensional rotational equation of motion can be expressed as in Eq. (14), where I_{yy} is the moment of inertia of both the canopy and the apparent mass, m is the mass of the canopy only, and g is the gravitational acceleration. Equation (14) can be rearranged to explicitly solve for the aerodynamic moment coefficients as seen in Eq. (15).

$$I_{yy}\ddot{a}_T = Q_w S_0 D_0 \begin{bmatrix} C_{m_{\dot{\alpha}}} & C_{m_\alpha} & C_{m_0} \end{bmatrix} \begin{bmatrix} \dot{\alpha}_T \frac{D_0}{2V_w} \\ \alpha_T \\ 1 \end{bmatrix} + mgR_{cp}\left[\cos\phi\cos\alpha_T\right] \tag{14}$$

$$\begin{bmatrix} C_{m_{\dot{\alpha}}} & C_{m_\alpha} & C_{m_0} \end{bmatrix} = \left(\frac{1}{Q_w S_0 D_0}\right)\left(I_{yy}\left[\ddot{a}_T\right] - mgR_{cp}\left[\cos\phi\cos\alpha_T\right]\right) \begin{bmatrix} \dot{\alpha}_T \frac{D_0}{2V_w} \\ \alpha_T \\ 1 \end{bmatrix}^T \left[\begin{bmatrix} \dot{\alpha}_T \frac{D_0}{2V_w} \\ \alpha_T \\ 1 \end{bmatrix} \begin{bmatrix} \dot{\alpha}_T \frac{D_0}{2V_w} \\ \alpha_T \\ 1 \end{bmatrix}^T \right]^{-1} \tag{15}$$

Equation (17) was simultaneously solved across a small range (or bin) of total angles of attack in order to obtain a set of coefficients that are representative of the parachute behavior within that α_T range. This bin was then incrementally stepped across the full range of α_T data in order to obtain a relatively smooth curve relating the moment coefficients to the total angle of attack. The resultant coefficients are assumed to correspond to the average total angle of attack within each bin. A larger bin size will result in a smoother curve, but it will tend to bias the resulting coefficients towards those angles of attack that occurred the most. The increment at which the bin is moved controls the density of points along the curve. The upper and lower bounds of the moment curves are limited by the angles that were traversed by the parachute during testing and the bin size selected.

D. Discussion of the Apparent Mass

Parachute aerodynamics are often hard to analyze because of complex interactions with the surrounding flowfield. For example, when a parachute is moving in a fluid, any external force that accelerates the parachute must also accelerate the fluid in and around the canopy. The fluid acceleration can be thought of as an additional mass of the system and is often referred to as the apparent mass. The effect of the apparent mass is very difficult to isolate since it is dependent on the fluid density, canopy size, canopy porosity, flow compressibility, and flow velocity. The apparent mass is often mathematically described as a 6x6 tensor with values based in both potential flow theory and empirical data.[8]

Ibrahim[9] performed a series of experiments to quantify the apparent inertia of rotating hemispherical, flat circular, guide surface, and ribbon canopies.[9] For each of the canopies, he determined a non-dimensional coefficient of the apparent moment of inertia for rotation around the canopy centroid as well as rotation around the canopy confluence point. The apparent inertia coefficient was non-dimensionalized with respect to a sphere of air of a diameter equal to the projected diameter of the canopy. Apparent inertias ranged from approximately 31% of a full sphere of air for a hemispherical canopy to 9% for a ribbon canopy. Uncertainty in these inertias was not documented.

Given the relatively small weight of the canopies and the high-density air at sea-level, the apparent inertia about the ball joint dominates the I_{yy} term in present analysis. Since the gravity term in Eq. (15) is much smaller than the aerodynamics term, the moment coefficients are approximately proportional to the apparent inertia. As a result, the apparent mass acts as a scaling factor on the calculated moment coefficients. This is a particularly important point since, as stated above, the correct apparent inertia value is very difficult to determine and the error in the calculated moment coefficients will be magnified by the error in the apparent inertia. Therefore, the results for the moment coefficients in Section IV are presented given the current best estimate of the apparent inertia.

IV. Results

Photogrammetric data was acquired for each canopy, although only a representative set of data are presented herein. For discussion purposes, Figs. 6-8 are presented for the RS-1 canopy at the 25 kt test condition. However, similar trends were also seen for the other canopies and conditions.

A. Two-Dimensional Canopy Motion

Figure 6 shows a two-dimensional trace of the canopy motion in the wind tunnel *yz*-plane (plane perpendicular to the wind tunnel centerline). The dots along the curve represent 3 Hz data and helps illustrate that a 60 Hz data rate provided a sufficiently dense sampling of the canopy motion. It can be seen that the parachute stays approximately within a circle of radius twenty feet, centered near the tunnel centerline. In addition, the parachute covers the entire interior of the circle fairly uniformly, showing that the canopy never develops a circular coning motion near its trim angle of attack. The parachute's time-averaged position in the *y*-direction is negligible and shows that there was no tendency for it to stay on either side of the test section. However, the average position in the *z*-direction is noticeably below zero, which can be attributed to gravity acting on the canopy.

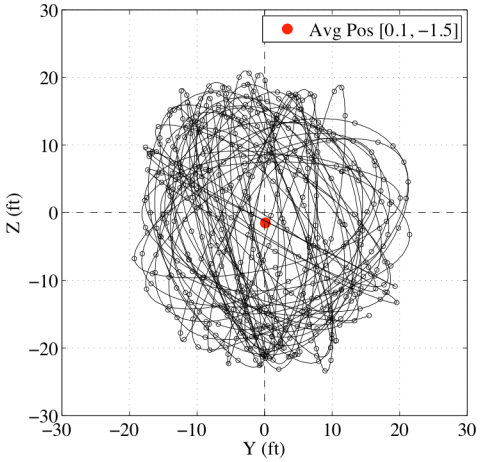

Figure 6. Trace of the RS-1 canopy vent.

B. Dynamic Versus Static Angle Contribution

The result of the total angle of attack calculation described in Section III.A is shown in Fig. 7. These plots show that the wind-relative angles are significantly greater the geometric angles due to rotation of the canopy. Additionally, Fig. 7b shows that the distributions of the angles change considerably. This is particularly important since the stability curves, which should be calculated based on total angle of attack, would look significantly different if based off of the total geometric angle. The mean and 95th percentile α_G and α_T are shown in Fig. 7b, which indicate that the wind-relative angles can be over 50% greater than the geometric angles.

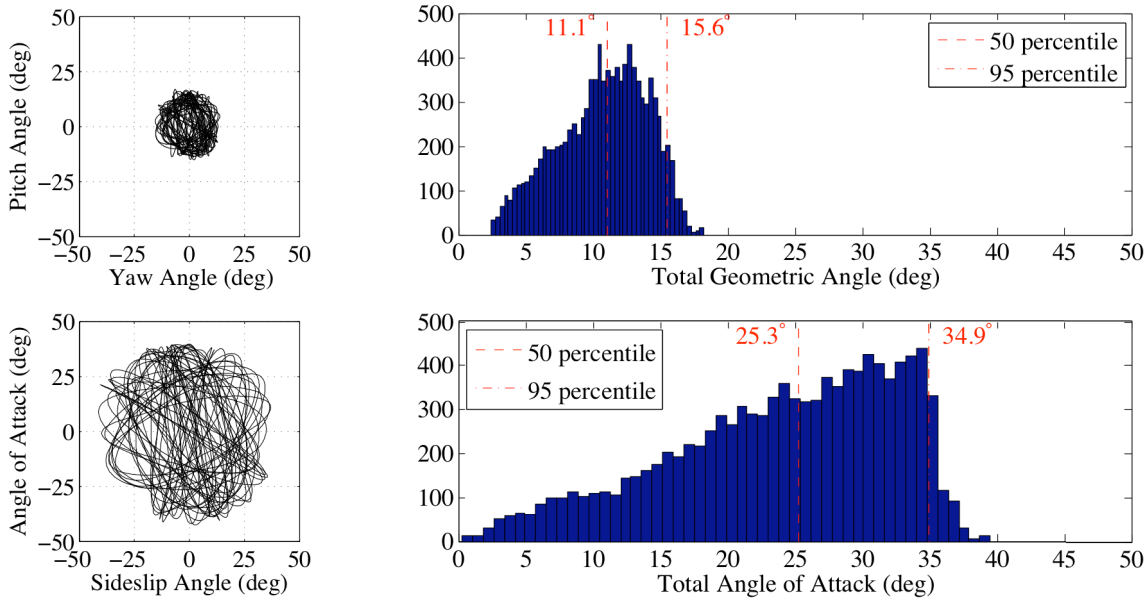

(a) Angular vent trace of the canopy motion over time

(b) Histogram of angles traversed by the parachute

Figure 7. Comparisons of the angular motion of the parachute when using geometric angles and wind-relative angles for the RS-1 canopy.

In addition, the use of wind-relative angles leads to a non-intuitive relationship between the total geometric angle and the total angle of attack. Figure 8a shows the tangential velocity of the canopy versus the total geometric angle at each point in the parachute trajectory. The tangential velocity is generally high at low total geometric angles and low at high angles. Thus, the parachute momentarily stops rotating when it reaches the maximum total angle of attack and rotates the fastest as it sweeps through the center, similar to simple harmonic motion. This means that the parachute reaches its largest total angle of attack just after passing through the center of the test section (α_G near zero). It then reaches the lowest total angle of attack just after attaining the maximum total geometric angle and starting its motion back to the center of the test section. In other words, the total geometric angle and the total angle of attack are approximately 180° out of phase from each other. This behavior can be seen in Fig. 8b.

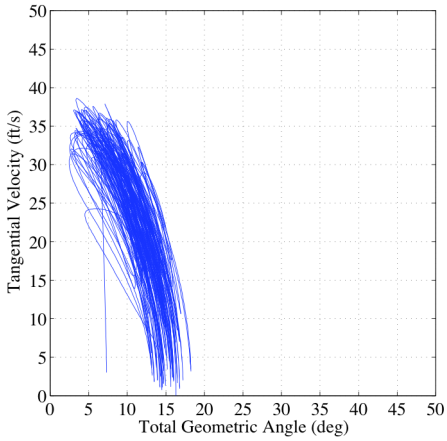

(a) Tangential velocity vs. total geometric angle

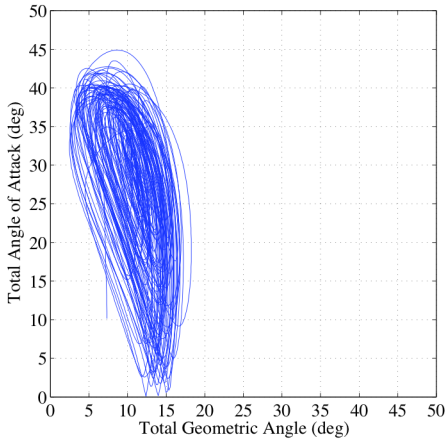

(b) Total angle of attack vs. total geometric angle

Figure 8. Comparisons between the tangential velocity and the total angle of attack profiles to the total geometric angle for the RS-1 canopy.

C. Raw Data Reduction and Processing

The stability coefficients were determined using a bin width of 0.5° and a bin step of 0.25°. The bin width was chosen because there were generally over 25 points contained within this bin size, which was assumed to be a sufficiently large sample size to generate representative coefficients. The bin step was chosen to provide an adequate number of data points from which to reconstruct the continuous C_m curve. A plot of the resultant C_m data for the RS-1 canopy is shown in Fig. 9 (both the blue circle and purple x symbols). These data were curve fit using an 8th order polynomial that was forced to go through a C_m of zero at 0° total angle of attack (which is typical of axisymmetric bodies). The data appeared to exhibit an unusually high C_m at low total angles of attack, thus some data were excluded from the fit, which are shown in the purple x symbols in Fig. 9. These curve fits will be used for the relative comparison of different canopies, although their absolute magnitudes may not be accurate due to the uncertainty in the apparent mass value used in the analysis. This topic is discussed further in Section IV.E.

The trim total angle of attack is the angle where the parachute does not experience an aero dynamic moment (C_m is equal to 0). A low trim angle of attack is desirable since it will be least likely to introduce a destabilizing moment on the payload and most of the drag force will be oriented along the centerline of the payload. For canopy RS-1, there are two trim angles – 0° and 23° total angle of attack. The positive moment curve slope at 0° is indicative of an unstable trim point, where a small perturbation will force the canopy away from its trim point. Conversely, the negative moment curve slope at 23° indicates a stable trim point, where any deviation of the parachute from this point will drive it back to the trim total angle of attack. The magnitude of $C_{m_{\alpha,trim}}$ determines the magnitude of the restorative force, or how stable the parachute is at the trim angle of attack. While a low trim angle of attack is always considered beneficial, it is not clear what is the best value for $C_{m_{\alpha,trim}}$. If moment curve slope is too low, then the restorative force is relatively weak and the parachute may traverse large angles during descent. However, if the moment curve slope is too large, then the parachute could potentially introduce a large, violent moment on the payload if it were suddenly displaced from the trim angle of attack due to a gust of wind or other perturbation. Another important feature of the curve is the peak C_m value. Higher peak values could also potentially cause violent motion and could cause destabilizing system

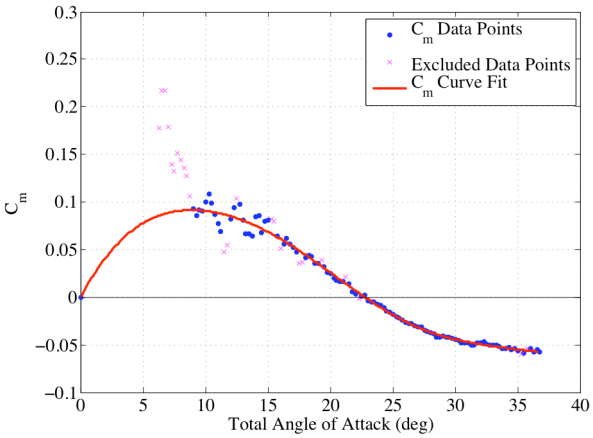

Figure 9. Static moment coefficients and curve fit as a function of the total angle of attack for the RS-1 canopy. X symbols were excluded when performing the curve fit.

dynamics. Therefore, a lower overall C_m curve is considered to be beneficial.

Figure 10 shows a plot of the pitch damping curve for the RS-1 canopy. To obtain a smooth curve it was necessary to increase the bin size to 1.5°. In the case of canopy RS-1, the pitch damping coefficient at the trim angle of attack is less than zero; therefore, the canopy is dynamically stable at the trim angle of attack. However, the results for the dynamic stability curves of different canopies vary widely and there is no overall trend regarding their dynamic stability. Like the static stability curve, the dynamic stability coefficients also start to scatter towards lower total angles of attack. However, this effect starts occurring at much higher angles than in the static curve. As a result, it is difficult to determine the shape of the pitch damping curve over the low values of total angle of attack, which makes comparisons between canopies difficult.

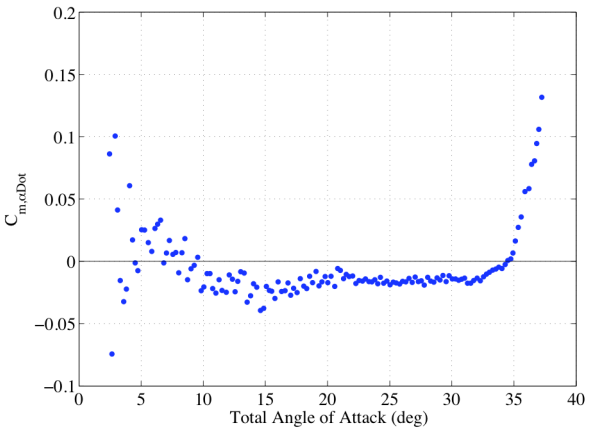

Figure 10. coefficients as a function of total angle of attack for the RS-1 canopy.

D. Comparison to Heritage Wind Tunnel Results

Prior to the Mars Exploration Rover missions, wind tunnel tests of various DGB parachutes were performed in the TDT to determine their drag performance and static stability behavior.[2] Moment values for each canopy was measured by constraining the parachute in a fixture that was rotated through a range of angles of attack. The data from this test have served as the basis of the parachute aerodynamics models for all subsequent U.S. Mars missions. In addition, the success of the DGB parachutes used in these missions demonstrates that these data are representative of Mars flight conditions and are the closest aerodynamics set to true parachute motion currently available. Therefore, it is useful to compare the results of the present NFAC test to the TDT test to ensure that the aerodynamics predicted by each test are not in conflict.

As part of the TDT test campaign, a sub-scale version of the Mars Viking DGB was flown that had a nominal diameter of approximately 5.2 ft and was constructed from MIL-C-7020 Type III. This test was run at sea-level density and a dynamic pressure of 16 psf. This canopy is very similar to the Mars Phoenix Scout canopy (DGB-1) flown in the present NFAC test. The Phoenix DGB gap and band heights were based on the Viking configuration and the fabric permeability of Type I and Type III MIL-C-7020 nylon are similar. However, the two DGB-1 tests were conducted at dynamic pressures of 0.8 and 2.5 psf. Figure 11 shows the resulting C_m curves from each of the tests.

Comparison between the TDT and NFAC tests is difficult because the runs were performed at very different dynamic pressures. Figure 11 shows how the data from the TDT (Viking DGB at 16 psf) vary from the present NFAC data (DGB-1 at 0.8 and 2.45 psf). The trim total angle of attack decreases with increasing dynamic pressure, although a reduction in the trim total angle of attack was also similarly observed in the TDT.[2] Additionally, the peak C_m and the general shape of the C_m curves appear to change with the dynamic pressure.

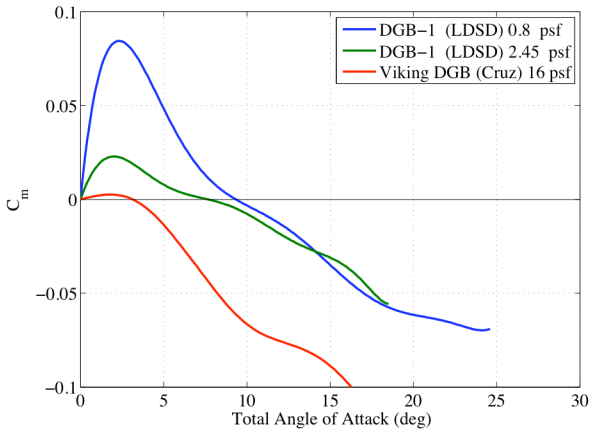

Figure 11. Comparison of C_m curves as a function of total angle of attack for wind tunnel tests performed in the NFAC and the TDT.

E. Apparent Mass Effects

The apparent mass is modeled as a coefficient multiplying the mass of a sphere of air of diameter equal to the parachute reference diameter. Referencing to a sphere of air causes the apparent moment of inertia to scale with the parachute diameter to the fifth power while the moment coefficients only scale with the diameter cubed. As a result, any error in the apparent mass model would be magnified for large diameter parachutes or muted for small parachutes. It has been seen that, despite the large differences in apparent mass, the TDT testing at sea level correlates well with Mars

flight data. Therefore, it could be that the small TDT test articles muted the effect of the apparent mass. The large parachutes flown by in NFAC, on the other hand, would amplify apparent mass effects and could be a contributing factor as to why the DGB-1 C_m curves are considerably different from the TDT curve in Fig. 11.

As stated in Section III.D, there is a considerable amount of uncertainty in how the apparent mass and apparent inertia are modeled. The apparent mass model scales with the density and size of the parachute, but does not account for dynamic pressure or canopy porosity. The lowest apparent inertia coefficient cited in reference 9 was 0.087, which was for a ringslot canopy with a geometric porosity of approximately 27%. As shown in Fig. 12, this apparent inertia coefficient generated a moment coefficient curve that was significantly different from the existing DGB data. Lacking sufficient information to intelligently vary the apparent inertia with dynamic pressure or canopy porosity, a constant apparent inertia coefficient value of 0.05 was used, which provided a slightly better correlation with the existing DGB data.

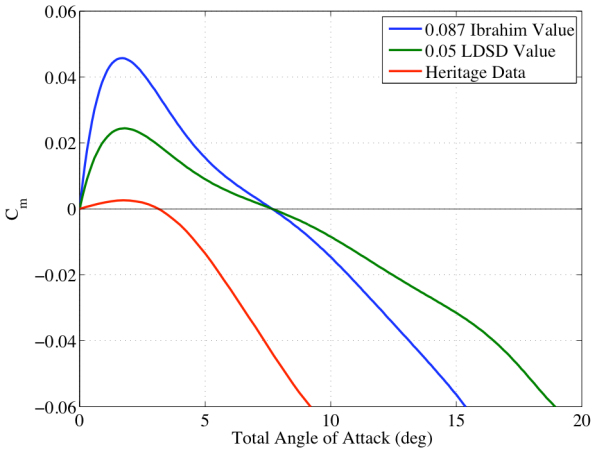

Figure 12. C_m curves calculated using varying apparent inertia coefficients for the DGB-2 canopy compared to heritage data.

F. Comparison Between Canopy Aerodynamics

The stability metrics for each canopy are tabulated in Table 1 along with their averaged drag and geometric porosity. Desirable canopies are ones that have low trim total angles of attack and high averaged tangential force coefficients (C_T). Since DGB parachutes have displayed acceptable stability behavior during prior U.S. Mars missions, the overall performance of each parachute can be determined in relation to the performance of the DGB (for example, equivalent stability with enhanced drag).

When comparing between the canopy test results two different effects are seen. The first is the effect of total porosity, where higher total porosity parachutes will generally be more stable and produce less drag than those with lower porosity. The second is the effect of porosity distribution, where certain canopies with advantageous porosity distributions will exhibit either higher stability or more drag than other canopies with equal total porosity. The results will be discussed in terms of geometric porosity since the total porosity is approximately equal to the geometric porosity due to the negligible fabric permeability of F-111 nylon. The one exception is the DGB-1 canopy, which was constructed from high permeability MIL-C-7020 Type I nylon.

Table 1. Summary of canopy stability and drag results.

Canopy Number	Canopy Description	Geometric Porosity (%)	Trim α_T (deg)	$C_{m_{\alpha,trim}}$ (1/deg)	Averaged C_T
DGB-1	DGB with high porosity fabric	13	8	-6×10^{-3}	0.59
DGB-2	DGB with low porosity fabric	13	15	-9×10^{-3}	0.81
RS-0	Ringsail design tested in 2005	10	23	-6×10^{-3}	0.99
RS-1	RS-0 without 2/3 ring 19	13	23	-8×10^{-3}	0.90
RS-2	RS-0 without 27% rings 17, 18, 19	15	24	-7×10^{-3}	0.91
RS-3	RS-0 without ring 19	16	21	-8×10^{-3}	0.86
RS-4	RS-0 without rings 18, 19	22	19	-11×10^{-3}	0.77
DS-0	Disksail as built	9	23	-9×10^{-3}	1.03
DS-1	DS-0 without 1/2 ring 11	11	19	-8×10^{-3}	0.98
DS-2	DS-0 without ring 11	13	13	-15×10^{-3}	0.92
DS-3	DS-0 without ring 11, 1/2 ring 17	16	12	-13×10^{-3}	0.86
DS-4	DS-0 without ring 11, 1/2 rings 17, 18	19	14	-10×10^{-3}	0.82
SS	Starsail as built	13	23	-5×10^{-3}	0.83

Figure 13 shows the static stability curves for the DGB-1 and DGB-2 canopies at the same dynamic pressure. While both canopies have the same geometric porosity, the DGB-1 has a higher total porosity (15-18%) than DGB-2. Figure 13 shows that higher fabric permeability effectively decreases the peak C_m value, decreases the trim α_T, and changes the overall shape of the curve. Similar behavior was also observed for canopies of differing total porosities in the aforementioned TDT test of DGB parachutes.[2]

Figure 14 shows a comparison of the moment coefficient curves for the unmodified ringsail, disksail, and starsail canopies as well as for the F-111 DGB. The three "sail" canopies all have approximately the same trim total angle of attack, which is significantly greater than the trim α_T of the DGB canopy.

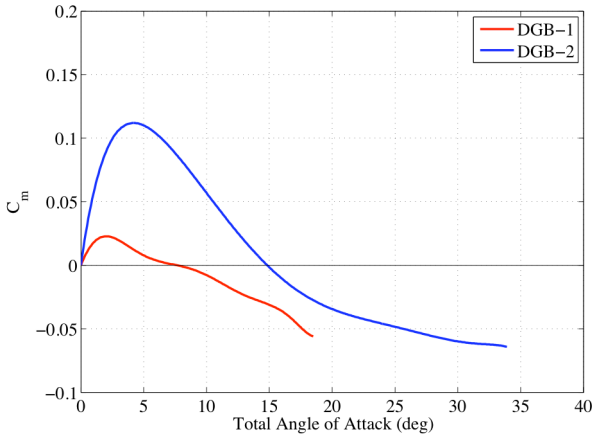

Figure 13. Comparison of C_m curves for the DGB canopies.

have and similar magnitude C_m curves across the entire range of total angle of attack but from Table 1, that the Disksail has slightly better drag performance. This is true for many of the modifications as well. (DS-0 has equivalent trim total angle of attack as the RS-0 and RS-1 but has higher drag. DS-1 has the same trim total angle of attack as the RS-3 but has much higher drag). Therefore, it appears as if the Disksail canopy is able to increase the drag of the Ringsail without significant reductions in stability. Comparisons of the $C_{m_{\alpha,trim}}$ values is difficult since it is uncertain what is an optimal value. However, it is known that a higher magnitude slope at the trim total angle of attack is more stable and the consistent success of DGB canopies in U.S. Mars missions implies that the slope of the DGB-2 C_m curve is not too high as to pose a danger to the system stability. Therefore, since the Disksail's $C_{m_{\alpha,trim}}$ is higher than that of the Ringsail but still less than that of the DGB-2 it is predicted that motion of the Disksail at the trim angle will not be overly violent and that its steeper $C_{m_{\alpha,trim}}$ is beneficial.

The Starsail canopy has a similar trim total angle of attack to the RS-0 and DS-0 but much lower drag. While it does have slightly better drag than the DGB-2 it also has a much higher trim total angle of attack. However, the Starsail C_m curve is very interesting and is quite different from the other canopies. It has a low magnitude C_m curve along the entire range of total angle of attack and a very shallow slope at the trim total angle of attack. This predicts that the canopy is not very stable at the trim angle but also does not experience significant forcing when away from the trim angle. Given that the Starsail is the only canopy without an even azimuthal distribution of porosity this shows that porosity concentrated along specific gores significantly changes the parachute interaction with the wind. However, given that the Disksail and Ringsail canopies had the same trim total angle of attack and much higher drag, the Starsail was considered to be a less effective design. (It should also noted that the unconventional design of the canopy also made it difficult to manufacture)

Based on the peak magnitude of the C_m curve and the low value of the trim total angle of attack in Fig. 14, DGB-2 appears to be more stable than both the unmodified Ringsail and Disksail canopies, but also has less drag. Since higher drag canopies are generally less stable, the stability of the Ringsail and Disksail canopies must first be improved before a meaningful comparison can be made. It is expected that any improvement in stability from an increase in geometric porosity will be coupled with a reduction in drag. However, intelligent modifications to the porosity distribution can potentially maximize the increase in stability with a minimal reduction in drag. In DGB canopies, the gap causes flow separation around the canopy and results in increased stability. Therefore, modifying the Ringsail or Disksail

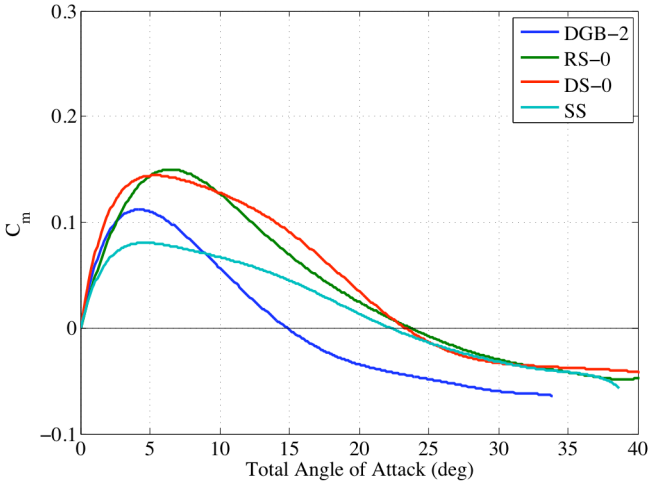

Figure 14. Comparison of the C_m curves for the unmodified canopies.

canopies to incorporate a similar gap feature could potentially improve their stability while maintaining much of their high drag performance.

This idea was employed when designing the canopy modifications. Panels were sequentially removed from rings located at various distances from the canopy skirt to see if preferencing the porosity distribution near or away from the skirt was advantageous. In addition, different azimuthal porosity distributions were investigated by removing either a full ring or every other panel. Given the time constraints of testing and the relatively poor performance of the baseline Starsail canopy, further modifications of the Starsail were not considered. Results for the Ringsail modifications are presented in Figs. 15a and 15b while results for the Disksail modifications are presented in Figs. 16a and 16b. The *Cm* curve for the DGB-2 canopy is provided in each figure as a reference.

With the exception of the RS-4 canopy, which was a completely separate parachute, each modification of the Ringsail (RS-2 through RS-4) was additive and successively increased total porosity. However, contradictory to the results in Fig. 13, as seen in Figs. 15a and 15b there is no direct correlation between the peak C_m value and total porosity. In particular, the reduction in the peak C_m value gained from RS-1 is subsequently lost in RS-2. The ½ ring of fabric on the RS-1 canopy was continually flapping during testing and was removed for canopy RS-2.[1] Therefore, it could have caused the dramatic reduction in the C_m value but there is not enough evidence for a conclusive answer.

Figure 15b shows a comparison of an increase in porosity distributed in different ways. Both RS-1 and RS-4 add porosity near the skirt of RS-0 but RS-1 adds all of it to ring 19 while RS-4 distributes the increase between rings 17, 18, and 19. Considering only the effect of increasing geometric porosity, RS-4 would be expected to have higher stability and lower drag (RS-4 has 15% geometric porosity while RS-1 has 13%). However, it can be seen that the magnitude of the C_m curve for the RS-1 canopy is lower than that of the RS-4 canopy over the entire range of total angle of attack. Therefore, RS-1 has a lower peak C_m value and trim total angle of attack. In addition, from Table 1, it can be seen that the RS-4 canopy has slightly higher drag. Thus, these results show that changes in geometric porosity distribution can have a large effect on canopy stability and drag. For porosity near the skirt, this predicts that geometric porosity distributed evenly is beneficial for drag while geometric porosity concentrated all in a single ring is beneficial for stability. This is similar to the results observed from the DGB-2.

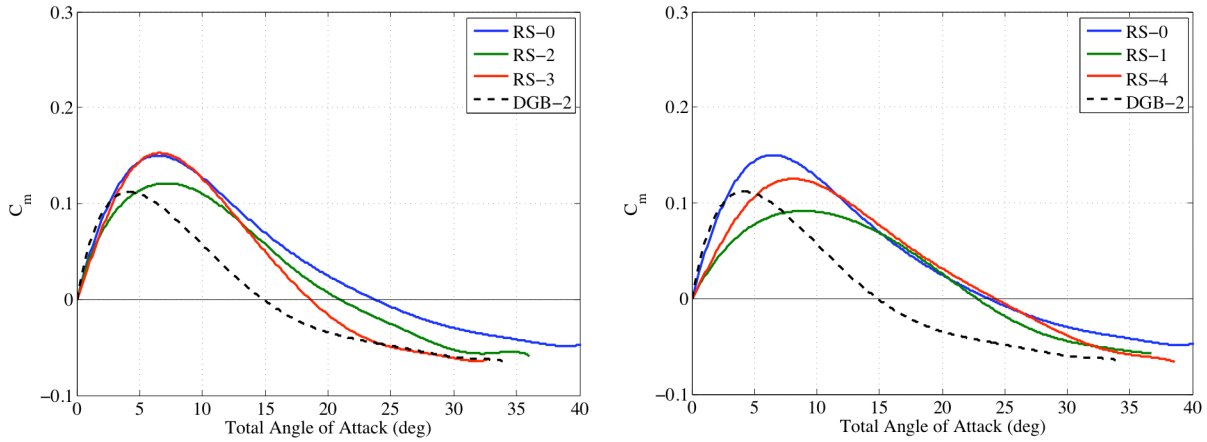

(a) Ringsail modifications part 1

(b) Ringsail modifications part 2

Figure 15. Comparison of C_m curves for the Ringsail canopy modifications

All of the modifications to the DS-0 canopy were additive and successively increased total porosity. As seen in Figs. 16a and 16b, the first two modifications (DS-2 and DS-3) have the smallest increase in total porosity but cause the highest reductions in the trim total angle of attack. While DS-4 further reduces the trim total angle of attack slightly, DS-5 causes it to increase. When considering only the trim total angle of attack, it seems as if increasing porosity near the crown of the parachute causes the highest increase in stability, though this is likely related to the fact that the baseline Disksail has no porosity in the crown.

While removing ring 11 (DS-2) has a significant effect on the trim total angle of attack, it also causes a large increase in the peak C_m value, which is retained in all further modifications. In fact, DS-3 has the highest peak C_m value of any canopy tested as well as the steepest slope at the trim angle. This shows that it is the most stable at the trim total angle of attack but could potentially cause violent motions if it is displaced from this point. However, DS-3 is a particularly attractive design since it has a low trim total angle of attack and high tangential force coefficient compared to the other canopies and their modifications. Therefore, it can be seen that the DS-3 canopy has very good drag and stability characteristics but could potentially be too stiff around the trim total angle of attack. An

alternative design is DS-2 which has a higher trim total angle of attack and peak C_m value than the DGB, but has a similar $C_{m_{\alpha,trim}}$ and much higher tangential force coefficient. Thus, the DS-2 canopy could potentially be described as having equivalent stability as the DGB with much higher drag.

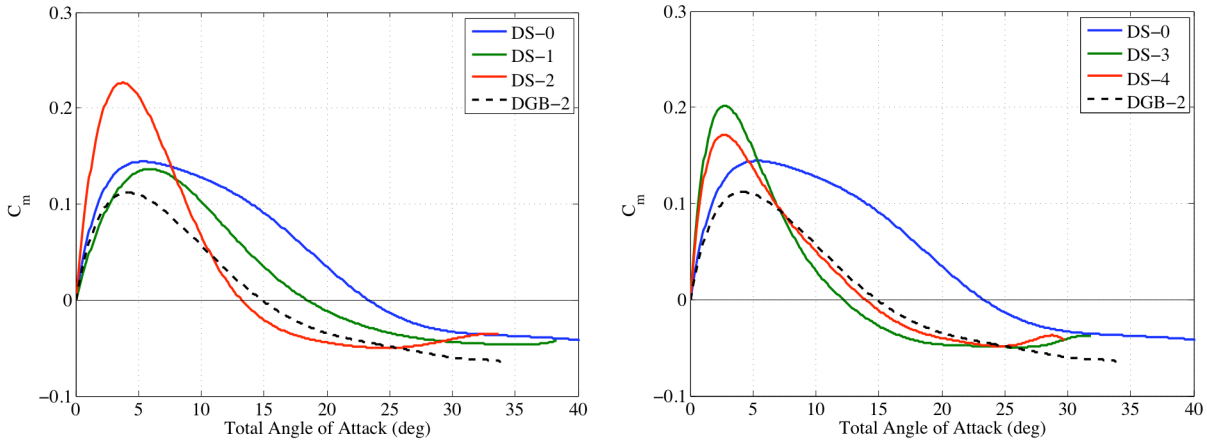

(a) Disksail modifications part 1 (b) Disksail modifications part 2

Figure 16. Comparison of C_m curves for the Disksail canopy modifications

V. Conclusion

The LDSD wind tunnel testing was able to quantitatively determine the aerodynamics of many different parachute canopy designs using video data of free flight tests. Photogrammetric imaging of the canopies during testing was used to track the vent and determine its position history. Retro-reflective targets placed on the canopy allowed for accurate determination of the vent location and extensive camera calibration and validation reduced the uncertainty in the calculated coordinates of the vent to less than 1 inch.

Geometric and wind relative angles were calculated from the canopy position history. It was found that the dynamic components of the angles of attack and sideslip were significant and heavily influenced the values of the total angle of attack. Motion of the canopy also led to a non-intuitive total angle of attack profile that was significantly different than the total geometric angle profile.

The equations of motion used to extract the moment coefficients from the canopy motion history required knowledge of the parachute properties and test conditions. However, there was a large uncertainty in the value of the apparent mass since it could not be directly determined from the test data. Instead, the apparent mass was modeled based on historical work and data correlation. Testing large parachutes at sea level density meant that the apparent mass was very high and that it dominated the rotational inertia of the canopy. Therefore, the uncertainties in the calculated stability coefficients were driven primarily by the uncertainty in the apparent mass value.

Static and dynamic moment data were calculated for each canopy. To allow for the efficient comparison between different parachute designs, each set of coefficients was fit to a curve. For high total angles of attack, the density of data points was sufficient to allow for an accurate fit. However, for low total angles of attack, the density and certainty in coefficient values decreased, which allowed for much more variability in the fitted curve. Stability metrics such as the trim angle of attack and slope at the trim angle were also determined to aid in the comparison.

The reduction results were compared with existing DGB data but differences in the dynamic pressure and parachute size made comparisons between the two tests difficult. The overall shape of the C_m curves was similar and the trend of decreasing trim angle of attack with increase dynamic pressure was observed independently in both tests. However, uncertainty in the apparent mass and the effects of scaling with parachute size inhibited the direct comparison of C_m values between the two tests.

The canopies were then compared based on their relative stability and drag performance. It was observed that the DGB canopy showed desirable stability characteristics while the Ringsail and Disksail canopies showed desirable drag characteristics. The Disksail was particularly attractive, however, since certain modifications outperformed the Ringsail and DGB canopies in both stability and drag. It seems as if the Starsail is not the best option since it was consistently outperformed in both stability and drag. However, recommendation of a final design will take into account the full aerodynamic and drag performance of each canopy as well as structural considerations and other parameters not captured in this analysis.

Appendix

A. Calculating the Total Angle of Attack

For ease of explanation, the current discussion assumes that motion is restricted to the pitch plane although theory for general motion will be developed later. The canopy rotation in the pitch plane is shown in Figs. 17a and 17b. V_t is the tangential velocity from the canopy rotation. It is important to measure the canopy velocity at the center of pressure (R_{cp}) since the aerodynamic forces act on this point. Therefore, V_t is calculated via Eq. (18). V_c is the axial wind velocity at the canopy, which is assumed to be in the same direction as V_∞ but can have a larger magnitude due to blockage effects. The resulting velocity triangle seen in Figs. 17c and 17d gives rise to the actual wind velocity (V_w) seen by the canopy and the dynamic angular component of the angle of attack. Note that positive V_t is defined as being in the directions denoted in Figs. 17c and 17d and is dependent on the sign of $\dot{\theta}$.

$$|V_t| = R_{cp}\dot{\theta} \tag{18}$$

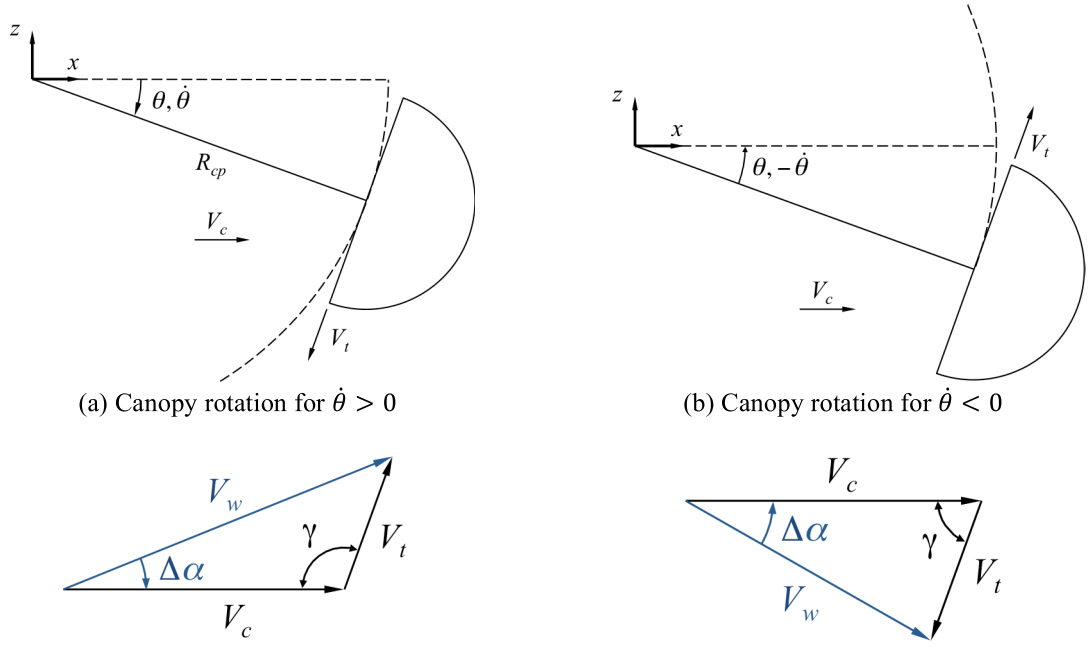

(a) Canopy rotation for $\dot{\theta} > 0$

(b) Canopy rotation for $\dot{\theta} < 0$

(c) Velocity triangle for $\dot{\theta} > 0$

(d) Velocity triangle for $\dot{\theta} < 0$

Figure 17. Diagram of canopy rotation and the resulting wind velocity triangle for motion in the pitch plane

γ is defined as the angle between V_c and V_T and can be solved geometrically via Eq. (19). In Eq. (19) sgn is the sign function where $sgn(\dot{\theta}) = 1$ for $\dot{\theta} > 0$ and $sgn(\dot{\theta}) = -1$ for $\dot{\theta} < 0$. Note that this expression is valid for both cases of $\dot{\theta} > 0$ and $\dot{\theta} < 0$.

$$\gamma = \frac{\pi}{2} + \mathrm{sgn}(\dot{\theta})\theta \tag{19}$$

γ, V_c and V_T fully define the velocity triangle so V_w can be solved via the Law of Cosines. The resulting expression for V_w is seen in Eqs. (20.1) and (20.2).

$$V_w^2 = V_c^2 + V_t^2 - 2V_cV_t\cos\gamma \tag{20.1}$$

$$V_w = \sqrt{V_c^2 + R_{cp}^2\dot{\theta}^2 - 2V_c\left|R_{cp}\dot{\theta}\right|\cos\left[\frac{\pi}{2} + \text{sign}\left(\dot{\theta}\right)\theta\right]} \tag{20.2}$$

With V_w, V_t, and γ known, $\Delta\alpha$ can be calculated via the Law of Sines. The resulting expression for $\Delta\alpha$ is seen in Eqs. (21.1) and (21.2).

$$\frac{\sin\Delta\alpha}{V_{t_\theta}} = \frac{\sin\gamma_\theta}{V_{w_\theta}} \tag{21.1}$$

$$\Delta\alpha = \sin^{-1}\left[\frac{\left|R_{cp}\dot{\theta}\right|}{\sqrt{V_c^2 + R_{cp}^2\dot{\theta}^2 - 2V_c\left|R_{cp}\dot{\theta}\right|\cos\left[\frac{\pi}{2} + \text{sgn}\left(\dot{\theta}\right)\theta\right]}}\sin\left[\frac{\pi}{2} + \text{sgn}\left(\dot{\theta}\right)\theta\right]\right] \tag{21.2}$$

The aerodynamic angle of attack is the sum of the geometric pitch angle and the dynamic contribution to the angle of attack. Thus, the angle of attack is calculated via Eqs. (22.1) and (22.2).

$$\alpha = \theta + \Delta\alpha \tag{22.1}$$

$$\alpha = \theta + \sin^{-1}\left[\frac{\left|R_{cp}\dot{\theta}\right|}{\sqrt{V_c^2 + R_{cp}^2\dot{\theta}^2 - 2V_c\left|R_{cp}\dot{\theta}\right|\cos\left[\frac{\pi}{2} + \text{sgn}\left(\dot{\theta}\right)\theta\right]}}\sin\left[\frac{\pi}{2} + \text{sgn}\left(\dot{\theta}\right)\theta\right]\right] \tag{22.2}$$

Since the parachute is axis-symmetric, motion in the yaw plane is equivalent to motion in the pitch plane. Thus, the derivation for the aerodynamic sideslip angle follows the same procedure as for the angle of attack resulting in Eq. (23).

$$\beta = \psi + \sin^{-1}\left[\frac{\left|R_{cp}\dot{\psi}\right|}{\sqrt{V_c^2 + R_{cp}^2\dot{\psi}^2 - 2V_c\left|R_{cp}\dot{\psi}\right|\cos\left[\frac{\pi}{2} + \text{sgn}\left(\dot{\psi}\right)\psi\right]}}\sin\left[\frac{\pi}{2} + \text{sgn}\left(\dot{\psi}\right)\psi\right]\right] \tag{23}$$

The total angle of attack is similar to the total geometric angle except it is computed from the aerodynamic angles instead of geometric angles and, as a result, takes into account the canopy rotation. The total angle of attack can be calculated via Eqs. (24.2) and (24.3) by recognizing that the two transformations (given in Eq. (24.1)) of the location of the canopy vent from the parachute frame to the wind tunnel frame are equivalent. Note that the total angle of attack is always positive due to its physical definition.

$$R_v\hat{x}' = R_v\cos\alpha\cos\beta\hat{x} = R_v\cos\alpha_T\hat{x} \tag{24.1}$$

$$\cos\alpha_T = \cos\alpha\cos\beta \tag{24.2}$$

$$\alpha_T = \cos^{-1}\left[\cos\alpha\cos\beta\right] \tag{24.3}$$

B. Calculating Derivatives of the Total Angle of Attack

The derivative of the total angle of attack can be calculated by taking the derivative of Eq. (24.2). $\dot{\alpha}_T$ can be found after taking the chain rule as seen in Eq. (25).

$$\dot{\alpha}_T = \frac{\dot{\alpha}\sin\alpha\cos\beta + \dot{\beta}\cos\alpha\sin\beta}{\sin\alpha_T} \tag{25}$$

The derivative of the angle of attack can be found from the differentiation of its definition in Eq. (22.1). The derivative of the sideslip angle can be found in the same manner. The expressions for the derivatives of the angles of attack and sideslip are seen in Eqs. (26.1) and (26.2).

$$\dot{\alpha} = \dot{\theta} + \Delta\dot{\alpha} \tag{26.1}$$

$$\dot{\beta} = \dot{\psi} + \Delta\dot{\beta} \tag{26.2}$$

The derivative of the dynamic contribution to the angle of attack can be found by differentiating Eq. (21.1) and is calculated via Eq. (27.1). The derivative of the dynamic contribution to the sideslip angle is found in the same way and is calculated via Eq. (27.2).

$$\Delta\dot{\alpha} = \frac{\dot{V}_{t_\theta} V_{w_\theta} - V_{t_\theta}\dot{V}_{w_\theta}}{V_{w_\theta}^2}\frac{\sin\gamma_\theta}{\cos\Delta\alpha} + \frac{V_{t_\theta}}{V_{w_\theta}}\frac{\cos\gamma_\theta}{\cos\Delta\alpha}\dot{\gamma}_\theta \tag{27.1}$$

$$\Delta\dot{\beta} = \frac{\dot{V}_{t_\psi} V_{w_\psi} - V_{t_\psi}\dot{V}_{w_\psi}}{V_{w_\psi}^2}\frac{\sin\gamma_\psi}{\cos\Delta\beta} + \frac{V_{t_\psi}}{V_{w_\psi}}\frac{\cos\gamma_\psi}{\cos\Delta\beta}\dot{\gamma}_\psi \tag{27.2}$$

The derivatives of the tangential canopy velocity in the pitch plane, $\dot{\gamma}_\theta$, and the actual wind velocity in the pitch plane can be found by differentiating Eqs. (18), (19) and (20.1) and are calculated via Eqs. (28.1.1), (28.1.2), and (28.1.3) respectively. The derivatives of the tangential canopy velocity in the yaw plane, $\dot{\gamma}_\psi$, and the actual wind velocity in the yaw plane can be found in the same way and are calculated via Eqs. (28.2.1), (28.2.2), and (28.2.3) respectively.

$$\dot{V}_{t_\theta} = R_{cp}\ddot{\theta} \tag{28.1.1}$$

$$\dot{\gamma}_\theta = \dot{\theta} \tag{28.1.2}$$

$$\dot{V}_{w_\theta} = \frac{\dot{V}_{t_\theta}\left(V_{t_\theta} - V_c\cos\gamma_\theta\right) + \dot{\gamma}_\theta V_c V_{t_\theta}\sin\gamma_\theta}{V_{w_\theta}} \tag{28.1.3}$$

$$\dot{V}_{t_\psi} = R_{cp}\ddot{\theta} \tag{28.2.1}$$

$$\dot{\gamma}_\psi = \dot{\psi} \tag{28.2.2}$$

$$\dot{V}_{w_\psi} = \frac{\dot{V}_{t_\psi}\left(V_{t_\psi} - V_c\cos\gamma_\psi\right) + \dot{\gamma}_\psi V_c V_{t_\psi}\sin\gamma_\psi}{V_{w_\psi}} \tag{28.2.3}$$

The second derivative of the total angle of attack can be calculated by twice differentiating Eq. (24.2). $\ddot{\alpha}_T$ can be solved for after taking the chain rule as seen in Eq. (29).

$$\ddot{\alpha}_T = \frac{\ddot{\alpha}\sin\alpha\cos\beta + \ddot{\beta}\cos\alpha\sin\beta + \left(\dot{\alpha}^2 + \dot{\beta}^2 - \dot{\alpha}_T^2\right)\cos\alpha_T - 2\dot{\alpha}\dot{\beta}\sin\alpha\sin\beta}{\sin\alpha_T} \tag{29}$$

The second derivative of the angle of attack can be found from twice differentiating Eq. (22.1). The second derivative of the sideslip angle can be found in the same manner. The expressions for the second derivatives of the angles of attack and sideslip are seen in Eqs. (30.1) and (30.2).

$$\ddot{\alpha} = \ddot{\theta} + \Delta\ddot{\alpha} \tag{30.1}$$

$$\ddot{\beta} = \ddot{\psi} + \Delta\ddot{\beta} \tag{30.2}$$

The second derivative of the dynamic contribution to the angle of attack can be found by twice differentiating Eq. (21.1) and is calculated via Eq. (31.1). The second derivative of the dynamic contribution to the sideslip angle is found in the same way and is calculated via Eq. (31.2).

$$\Delta\ddot{\alpha} = \frac{1}{\cos\Delta\alpha}\left[\begin{array}{l}\dfrac{\left(\ddot{V}_{t_\theta}V_{w_\theta} - V_{t_\theta}\ddot{V}_{w_\theta}\right)\left(V_{w_\theta}^2\right) - \left(\dot{V}_{t_\theta}V_{w_\theta} - V_{t_\theta}\dot{V}_{w_\theta}\right)\left(2V_{w_\theta}\dot{V}_{w_\theta}\right)}{V_{w_\theta}^4}\sin\gamma_\theta + \\ 2\dfrac{\dot{V}_{t_\theta}V_{w_\theta} - V_{t_\theta}\dot{V}_{w_\theta}}{V_{w_\theta}^2}\dot{\gamma}_\theta\cos\gamma_\theta + \dfrac{V_{t_\theta}}{V_{w_\theta}}\left(\dot{\gamma}_\theta^2\sin\gamma_\theta + \ddot{\gamma}_\theta\cos\gamma_\theta\right) + \Delta\dot{\alpha}^2\sin\Delta\alpha\end{array}\right] \tag{31.1}$$

$$\Delta\ddot{\beta} = \frac{1}{\cos\Delta\beta}\left[\begin{array}{l}\dfrac{\left(\ddot{V}_{t_\psi}V_{w_\psi} - V_{t_\psi}\ddot{V}_{w_\psi}\right)\left(V_{w_\psi}^2\right) - \left(\dot{V}_{t_\psi}V_{w_\psi} - V_{t_\psi}\dot{V}_{w_\psi}\right)\left(2V_{w_\psi}\dot{V}_{w_\psi}\right)}{V_{w_\psi}^4}\sin\gamma_\psi + \\ 2\dfrac{\dot{V}_{t_\psi}V_{w_\psi} - V_{t_\psi}\dot{V}_{w_\psi}}{V_{w_\psi}^2}\dot{\gamma}_\psi\cos\gamma_\psi + \dfrac{V_{t_\psi}}{V_{w_\psi}}\left(\dot{\gamma}_\psi^2\sin\gamma_\psi + \ddot{\gamma}_\psi\cos\gamma_\psi\right) + \Delta\dot{\beta}^2\sin\Delta\beta\end{array}\right] \tag{31.2}$$

The second derivatives of the tangential canopy velocity in the pitch plane, $\ddot{\gamma}_\theta$, and the actual wind velocity in the pitch plane can be found by twice differentiating Eqs. (18), (19) and (21.1) and are calculated via Eqs. (32.1.1), (32.1.2), and (32.1.3) respectively. The second derivatives of the tangential canopy velocity in the yaw plane, $\ddot{\gamma}_\psi$, and the actual wind velocity in the yaw plane can be found in the same way and are calculated via Eqs. (32.2.1), (32.2.2), and (32.2.3) respectively.

$$\ddot{V}_{t_\theta} = R_{cp}\ddot{\theta} \tag{32.1.1}$$

$$\ddot{\gamma}_\theta = \ddot{\theta} \tag{32.1.2}$$

$$\ddot{V}_{w_\theta} = \frac{1}{V_{w_\theta}}\left[\dot{V}_{t_\theta}^2 + \ddot{V}_{t_\theta}\left(V_{t_\theta} - V_c\cos\gamma_\theta\right) + 2\dot{\gamma}_\theta V_c\dot{V}_{t_\theta}\sin\gamma_\theta + V_c V_{t_\theta}\left(\ddot{\gamma}_\theta\sin\gamma_\theta + \dot{\gamma}_\theta^2\cos\gamma_\theta\right) - \dot{V}_{w_\theta}^2\right] \tag{32.1.3}$$

$$\ddot{V}_{t_\psi} = R_{cp}\ddot{\psi} \tag{32.2.1}$$

$$\ddot{\gamma}_\psi = \ddot{\psi} \tag{32.2.2}$$

$$\ddot{V}_{w_\psi} = \frac{1}{V_{w_\psi}}\left[\dot{V}_{t_\psi}^2 + \ddot{V}_{t_\psi}\left(V_{t_\psi} - V_c\cos\gamma_\psi\right) + 2\dot{\gamma}_\psi V_c\dot{V}_{t_\psi}\sin\gamma_\psi + V_c V_{t_\psi}\left(\ddot{\gamma}_\psi\sin\gamma_\psi + \dot{\gamma}_\psi^2\cos\gamma_\psi\right) - \dot{V}_{w_\psi}^2\right] \tag{32.2.3}$$

C. Local Wind Velocity at the Canopy

The parachute center of pressure can be expressed in the inertial frame via the transformation matrix in Eq. (1). The inertial coordinates of the center of pressure are found in Eq. (33).

$$\mathbf{R}_{cp} = R_{cp}\begin{bmatrix} \cos\theta\cos\psi \\ \sin\psi \\ -\sin\theta\cos\psi \end{bmatrix} \tag{33}$$

The inertial angular velocity of the canopy can be determined by transforming the geometric angular rates via Euler transformation matrixes as seen in Eqs. (34.1) and (34.2). For a geometric interpretation of inertial angular velocity, see Fig. 4.

$$\boldsymbol{\Omega} = \begin{bmatrix} \cos\theta & 0 & \sin\theta \\ 0 & 1 & 0 \\ -\sin\theta & 0 & \cos\theta \end{bmatrix}\begin{bmatrix} 0 \\ \dot{\theta} \\ 0 \end{bmatrix} + \begin{bmatrix} \cos\theta & 0 & \sin\theta \\ 0 & 1 & 0 \\ -\sin\theta & 0 & \cos\theta \end{bmatrix}\begin{bmatrix} \cos\psi & -\sin\psi & 0 \\ \sin\psi & \cos\psi & 0 \\ 0 & 0 & 1 \end{bmatrix}\begin{bmatrix} 0 \\ 0 \\ \dot{\psi} \end{bmatrix} \tag{34.1}$$

$$\boldsymbol{\Omega} = \begin{bmatrix} \dot{\psi}\sin\theta \\ \dot{\theta} \\ \dot{\psi}\cos\theta \end{bmatrix} \tag{34.2}$$

Knowing the inertial coordinates of the parachute center of pressure and the inertial angular velocity, the tangential velocity of the canopy can be determined via Eqs. (35.1) and (35.2).

$$\mathbf{V}_t = \boldsymbol{\Omega} \times \mathbf{R}_{cp} \tag{35.1}$$

$$\mathbf{V_t} = \begin{bmatrix} \dot{x}_{cp} \\ \dot{y}_{cp} \\ \dot{z}_{cp} \end{bmatrix} = R_{cp}\begin{bmatrix} -\dot{\theta}\sin\theta\cos\psi - \dot{\psi}\cos\theta\sin\psi \\ \dot{\psi}\cos\psi \\ -\dot{\theta}\cos\theta\cos\psi + \dot{\psi}\sin\theta\sin\psi \end{bmatrix} \tag{35.2}$$

The total wind velocity at the canopy is the sum of the freestream wind velocity and the wind velocity due to tangential motion of the canopy as seen in Eq. (36.1). Note that the wind velocity due to the motion of the canopy is the negative of V_t since it acts in the opposite direction. The parameter of interest, V_w, is the magnitude (L^2- norm) of the total wind velocity vector ($\boldsymbol{V_w}$) and can be found via Eq. (36.2).

$$\mathbf{V}_w = \begin{bmatrix} V_c \\ 0 \\ 0 \end{bmatrix} - \begin{bmatrix} \dot{x}_{cp} \\ \dot{y}_{cp} \\ \dot{z}_{cp} \end{bmatrix} = \begin{bmatrix} V_c + R_{cp}(\dot{\theta}\sin\theta\cos\psi + \dot{\psi}\cos\theta\sin\psi) \\ -R_{cp}\dot{\psi}\cos\psi \\ R_{cp}(\dot{\theta}\cos\theta\cos\psi - \dot{\psi}\sin\theta\sin\psi) \end{bmatrix} \tag{36.1}$$

$$V_w = \sqrt{\left(V_c - \dot{x}_{cp}\right)^2 + \dot{y}_{cp}^2 + \dot{z}_{cp}^2} \tag{36.2}$$

Acknowledgments

This research was directed by the Jet Propulsion Laboratory, California Institute of Technology, under a contract with the National Aeronautics and Space Administration. The authors would like to thank Mark Schoenenberger and Juan Cruz for their insight on the data reduction improvements and final results was invaluable.

References

[1] Tanner, C., Clark, I., Gallon, J., Rivellini, T., and Witkowski, A., "Aerodynamic Characterization of New Parachute Configurations for Low-Density Deceleration," 22nd AIAA Aerodynamic Decelerator Systems Conference, Daytona Beach, CA, March 2013.

[2] Cruz, J. R., Mineck, R., Keller, D., and Bobskill, M., "Wind Tunnel Testing of Various Disk-Gap-Band Parachutes," AIAA Aerodynamic Decelerator Systems Technology Conference and Seminar, AIAA 2003-2129, May 2003.

[3] Schoenenberger, M., Queen, E. M., and Cruz, J. R., "Parachute Aerodynamics from Video Data," AIAA Aerodynamic Decelerator Systems Technology Conference and Seminar, AIAA 2005-1633, May 2005.

[4] Mitcheltree, R., Burno, R., Slimko, E., Ba_es, C., Konefat, E., and Witkowski, A., "High Altitude Test Program for a Mars Subsonic Parachute," AIAA Aerodynamic Decelerator Systems Technology Conference and Seminar, AIAA 2005-1659, May 2005.

[5]Kushner, L.K. and Schairer, E.T., "Planning Image-Based Measurements in Wind Tunnels by Virtual Imaging," AIAA Paper 2011-0930, presented at 49th AIAA Aerospace Sciences Meeting and Exhibit, Orlando, FL, Jan. 2011.

[6] Abdel-Aziz, Y.I. and Karara, H.M., "Direct Linear Transformation from comparator coordinates into object-space coordinates," Proceedings, Symposium on Close-Range Photogrammetry, American Society of Photogrammetry, Urbana, IL, Jan. 1971.

[7]McBride, D. D., "Orbiter Drag Chute Stability Test in the NASA Ames 80x120 Foot Wind Tunnel," Tech. Rep. SAND-93-2544, Sandia National Laboratories, Albuquerque, NM, Feb. 1994.

[8] Cockrell, D., Doherr, K. F., "Preliminary Consideration of Parameter Identification Analysis from Parachute Aerodynamic Flight Test Data," AIAA Paper 1981-1940, AIAA Aerodynamic Decelerator and Balloon Technology Conference, Oct. 1981.

[9] Ibrahim, S. K., "Experimental Determination of the Apparent Moment of Inertia of Parachutes," Tech. Rep. AFFDL-TDR-64-153, Air Force Flight Dynamics Laboratory, Wright-Patterson Air Force Base, Ohio, April 1965.